

Surface band bending in semimetal T_d -WTe₂

Aixi Chen

Suzhou Institute of Nano-tech and Nano-bionics

Huifang Li

Suzhou Institute of Nano-tech and Nano-bionics

Rong Huang

Suzhou Institute of Nano-tech and Nano-bionics

Yanfei Zhao

Suzhou Institute of Nano-tech and Nano-bionics

Tong Liu

Suzhou Institute of Nano-tech and Nano-bionics

Zhiyun Li

Suzhou Institute of Nano-tech and Nano-bionics

Li Wang

Suzhou Institute of Nano-tech and Nano-bionics

Feiyu Cheng

Suzhou Institute of Nano-tech and Nano-bionics

Wei Ren

Suzhou Institute of Nano-tech and Nano-bionics

Shuai Lu

Suzhou Institute of Nano-tech and Nano-bionics

Bingjie Yang

Suzhou Institute of Nano-tech and Nano-bionics

Zengli Huang

Suzhou Institute of Nano-tech and Nano-bionics

Sunan Ding

Suzhou Institute of Nano-tech and Nano-bionics

Fang-Sen Li (✉ fsli2015@sinano.ac.cn)

Suzhou Institute of Nano-tech and Nano-bionics

Research Article

Keywords: WTe₂ devices, electric polarization, ferroelectric switching

Posted Date: December 9th, 2020

DOI: <https://doi.org/10.21203/rs.3.rs-117815/v1>

License:  This work is licensed under a Creative Commons Attribution 4.0 International License.

[Read Full License](#)

Abstract

Recently, spontaneous out-of-plane electric polarization and ferroelectric switching were found in WTe_2 devices. On single crystal with ferroelectric property, a built-in electric field and corresponding band bending would be expected at the surface. However, such band bending in WTe_2 hasn't directly been observed experimentally. Here, by fitting angle-dependent X-ray photoelectron spectroscopy (XPS) spectra on WTe_2 surface, we clearly observed downward band bending after slightly exposure to air, verifying appearance of surface polarization. Such band bending can't be observed on pristine WTe_2 surface and will disappear on fully oxidized sample. It suggests strong correlation between surface band bending and oxidation. Ionized donors from oxide species pinned at surface may contribute to the formation of surface band bending and polarization. Our study here offers new insight to figure out the microscopic origin of ferroelectric in WTe_2 .

Introduction

As a layered transition metal dichalcogenide (TMD), tungsten ditelluride (WTe_2) crystallizes in a distorted orthorhombic structure (space group: $\text{Pnm}2_1$), named $T_d\text{-WTe}_2$ here. Both bulk and monolayer $1T\text{-WTe}_2$ have spurred tremendous studies due to intriguing properties, including large magnetoresistance,^{1,2} nonlinear anomalous Hall effect,³ superconductivity,⁴⁻⁷ quantum spin Hall behavior⁸⁻¹⁰ and type-II Weyl semimetal.¹¹⁻¹³ Recently, spontaneous out-of-plane electric polarization and ferroelectric switching were observed in two- and three-layer WTe_2 .¹⁴ Ferroelectricity and dipole can be tuned by electrically driven stacking transitions in few-layer WTe_2 .¹⁵ Switchable spontaneous polarization with natural ferroelectric domain structures¹⁶ was also found in WTe_2 bulk, which is polar with non-centro-symmetric structure. Their DFT calculation suggests polarization is pristine in such polar semimetal due to contribution from ionic cores and valence bands.¹⁶ However, experimental study about the origin of such polarization is still seldom. Normally, out-of-plane spontaneous polarization in single crystal should induce surface charge redistribution and built-in electric fields, which result into band bending near surface.¹⁷ Therefore, surface band bending can be a evidence for existence of polarization or ferroelectric on WTe_2 . Angle resolved photoemission spectroscopy (ARPES) measurements¹⁸⁻²¹ on freshly cleaved WTe_2 haven't shown such band bending. If exposing WTe_2 to air for 3 hours, J. M. Woods *et al.*²² observed decreased work function by 300 meV, which was claimed to be due to surface band bending.

If exposure to air, the surface of $T_d\text{-WTe}_2$ is easy to be oxidized.^{15,21-29} Investigation of its oxidation behavior is important for WTe_2 -based devices in real application, because surface oxidation will decrease conductivity,²³ suppress magnetoresistance²²⁻²⁶ and induce weak antilocalization.^{24,25} Strong oxidation happens within a few minutes,^{24,27} but the WTe_2 oxidation is self-limiting process and occurs mostly on the top surface. A thin surface oxide layer (~ 2 nm thick^{16,22}) can be quite effective to protect inner bulk layer from further degradation. The reason is still unknown. According to XPS measurements,^{22,23,26-28}

the oxidation driving force are formation of WO_x and TeO_x on the surface of WTe_2 . Theoretical calculation^{24,29} claimed the fast oxidation happens with the aid of H_2O , which can decrease the reaction barrier. And charge depletion was found to near the O adsorption site, which may induce charge dipolar and even polarization.

In spite of many investigations about oxide behavior of WTe_2 , oxidation dynamic and how the oxidation affects the electron band structure are seldom to be studied. Here we combined angle-dependent X-ray photoelectron spectroscopy (ADXPS) and TOF-SIMS to investigate the exposure-time-dependent oxidation behavior and surface band bending. We found the oxidized species were WO_3 and TeO with oxygen vacancies, which protect deeper layer to be oxidized. What's more, we observed clear downward surface band bending, confirming the out-of-plane polarization on WTe_2 . Further we found the surface band bending is closely related to surface oxidation.

Results And Discussion

Among TMDs, WTe_2 crystallizes to T_d phase energetically with an additional structural distortion: the tungsten atoms form quasi one-dimensional zigzag chains along a direction and Tellurium atoms form undulation morphology, as show in Fig. 1a. The thickness of Te-W-Te is ~ 0.42 nm and the space between neighboring van der Waals interacting layer is ~ 0.29 nm. Before ADXPS measurements, we have systematically studied the oxidation behavior by combined XPS, TEM and TOF-SIMS. Scanning X-ray Induced Secondary Electron Image (SXI) was adopted to locate and trace the probe area with size of ~ 100 μm , as shown in the inset of Fig. 1b. Figure 1c shows the normalized XPS spectra of Te 3d core level, collected at TOA of $\theta = 45^\circ$. Only two Te 3d peaks (Te 3d_{5/2}-W and Te 3d_{3/2}-W) with splitting energy of 10.39 eV were observed after UHV cleavage. No trace of C and O signal indicates free of oxidation. After exposure to air for one minute, a small shoulder appears at about 576 eV, which is the Te 3d_{5/2}-O peak. We used the ratio of shoulder to main peak of Te 3d_{5/2}-W to estimate the oxidation degree. The oxidation ratio is only $\sim 2\%$. When increasing exposure to 5 min, the Te-O peak are pronounced and the ratio quickly increases to $\sim 16.6\%$. Further exposures only induce slightly increased oxidation to $\sim 19.2\%$, as shown in Fig. 1d. It suggests WTe_2 oxidizes quickly after exposure to air, within few mins, and the oxidation is self-limited process without deep oxidation, consistent with previous Raman measurements.^{24,27} We found the core level of Te 3d_{5/2}-W shifted after exposure, which will be discussed in Fig. 4d.

The HRTEM image in the left panel of Fig. 2a shows after long-time exposure, a thin amorphous oxide layer with slight weak intensity can be found between WTe_2 and deposited Pt protective layer. EELS line profile in Fig. 2c and mapping image in the Fig. 2b suggest the thickness of oxidation layer is ~ 2.4 nm, agreeing with previous estimation.^{16,22} It means the top four WTe_2 layers are nearly oxidized after long time exposure. We must point out that due to the integration of photoelectrons emitting from a depth of d_0 , oxidation ratio obtained from XPS measurements is $\sim 19.2\%$. Trace of some weak layered structure still can be identified. Such amorphous layer is uniform and dense, which can block the entrance of O_2

and H₂O to avoid further oxidation. Information about the proportion of elements after oxidation is helpful to understand the oxidation dynamic. To illustrate the components of oxidation layer, we performed delicate TOF-SIMS measurements according to the depth profile of different negative fragments, as shown in Fig. 2d. For tungsten species (WO₃⁻, WO₂⁻, WO⁻ and W⁻), we find the WO₃⁻ has the largest intensity and nearly ten times more than that of WO₂⁻. The depth profile of both WO₃⁻ and WO₂⁻ show a peak behavior near surface. In addition, the core level of W 4f_{7/2}-O peak is about 35.5 eV (not shown here), agreeing with the peak energy in WO₃ (NIST database,³⁰ 35.8 eV ± 0.4 eV, while the one in WO₂ is 32.9 eV ± 0.8 eV). These facts indicate the main oxidation component of W here is WO₃. For tellurium species (TeO₃⁻, TeO₂⁻, TeO⁻ and Te⁻), the intensity of TeO⁻ is nearly 8 times more than that of TeO₂⁻. Although the formation of species during TOF-SIMS measurement is a very complicated process and the sputtering yields or intensities are related to real concentration and secondary ionization rate, we find here only TeO⁻ intensity shows a peak behavior similar to WO₃⁻. We conclude that the main oxidation component of Te is TeO. We notice that the core level of Te 3d_{5/2}-O is about 576.2 eV, within the peak energy range in TeO₂ (NIST database,³⁰ 576.1 eV ± 0.3 eV, while the one in TeO₃ is 577.0 eV ± 0.5 eV). Normally for tellurium element, TeO₂ is the stable oxidation state. The observation of main TeO component here suggests the oxidation layer is oxygen deficit, which thus prevents the deep WTe₂ layer to be oxidized.

To figure out the band structure evolves after oxidation, we systematically performed ADXPS measurements after each exposure. Figure 3a shows a series of spectra on UHV cleaved sample at different emission angles of θ . We can't find any trace of oxidation signal even at $\theta = 20^\circ$. The intensity increases with emission angles θ , while the core level of Te 3d_{5/2}-W keeps almost constant at different TOAs, as shown in Fig. 3c. The photoelectron escape depth λ depends on the TOA (θ) in a simple relation of $\lambda_0 \sin(\theta)$, where λ_0 is the inelastic mean free path of photoelectrons. The value of λ_0 is 3.25 nm for photoelectrons of Te 3d in WTe₂, as calculated by TPP-2M method³¹ in NIST's database.³² After exposure to air for one minute, Te-O bond can be observed at each emission angle in Fig. 3d. We find obvious binding energy shift in Fig. 3f. After subtracting Shirley background, the spectra collected under different TOAs were fitted using Eqs. (1) and (2) in Method with the fitting parameters: binding energy E_0 , strength of the electrostatic potential K , the ratio of Gaussian function α , and the full width at half maximum F . The fitted curves were displayed in Fig. 3b and Fig. 3e. For UHV cleaved sample, the resulted fitting parameters are $E_0 = 572.97$ eV, $K = -0.0112$ eV/nm, $\alpha = 0.404$ and $F = 1.01$ eV. The small K suggests the surface band bending can be negligible on fresh cleaved surface, consistent with previous ARPES measurements.¹⁸⁻²¹ However, on one min-exposure sample, the strength of electrostatic potential K decreases to -0.0358 eV/nm with $E_0 = 573.00$ eV, $\alpha = 0.396$ and $F = 1.25$ eV. Taking the obtained fitting parameters back into Eqs. (1) and (2), we can draw the simulation curve as function of TOAs, as shown in Fig. 3c and 3f. The negative value of K suggests the surface band is bending downward.

When exposing to air for 5 min, the strength of electrostatic potential K further decreases to -0.0576 eV/nm, but the fitting error is large according to the simulation curve in Fig. 4a. Such large error is probably due to quick oxidation and nonuniform charge distribution at the first stage of 5 min. Nevertheless, increased electrostatic potential or band bending is obvious. After exposure to air for more than 32 hours in Fig. 4b, the binding energy nearly keeps constant again at different TOAs and the value of K increases back to near zero. We summarize the strength of surface electrostatic potential as function of exposure time in Fig. 4c. Clear close correlation between surface oxidation and surface electrostatic potential or surface downward band bending is found.

According to the carrier density and dielectric constant of WTe_2 in Poisson's Eq. 2², the depletion layer or spatial extent of the band bending is estimated to be $1 \sim 2$ nm. We notice that previous two experimental observations of ferroelectricity were performed in glove box with N_2 protective gas. Considering the rapid oxidation behavior, the surface of WTe_2 was expected to be in analogy with the one of one-minute-exposed samples, where the strength of electrostatic potential is -0.0358 eV/nm. It means the built-in electric field potential should be ~ 36 meV, which agrees well with the estimated changes in potential difference for polarization reverse ($2\delta V \approx 40$ meV) in previous report.¹⁴ Further, previous observed ferroelectric domain structure during piezo response force microscopy measurement¹⁶ has distorted circular profile with size of $20 \sim 50$ nm and decoratively distributed on the surface. Considering the orthorhombic symmetry of T_d - WTe_2 and our observation of surface built-in electric field, the distorted circular may be oxidized defects with amorphous structure. Although we conclude the close correlation between surface polarization and surface oxidation, the detailed microscopic mechanism for ferroelectricity after oxidation in WTe_2 deserves further investigation.

We would like to discuss about how the surface oxidation affects the amount of band bending. Surface of freshly cleaved sample has the same size of electron pockets and hole pockets across Fermi level (E_F) with perfect electron - hole charge compensation. As expected, negligible band bending was observed with small K in our ADXPS measurement. When the surface starts to oxidize, the oxidation species (WO_x and TeO_x) will induce hole doping due to the high work function. At the beginning, oxidation happens locally (such as vacancies) with the ionized donors pinned on the surface, as shown in the schematic diagram in Fig. 4e. The pinned donor will attract the electrons and then form built-in electric field (E) pointing to the bulk. It agrees with the previous observation of polarization on WTe_2 surface.^{14,16} However, here we show the oxidation effect induces such polarization rather than its intrinsic property. Due to the pinned ionized donors, the attracted electrons below oxide layer will shift the core-level to higher binding energy. It agrees with the peak shift observation in Fig. 4d. When the surface further oxidizes after long time exposure, the oxidation layer becomes thick and nonlocalized, which can't pin the donor again. On the contrary, the oxidation layer induces nonlocal hole doping to compensate the attracted electrons, then results into weakened surface band bending. Such hole doping agrees with the shift the core-level to lower binding energy when the exposure time increase to 2 h and 32 h in Fig. 4d.

Conclusion

In summary, we have systematically studied the oxidation behavior of WTe_2 and probed the changes of surface band structure by using angle-dependent XPS. WTe_2 oxidizes quickly after exposure to air for 5 min. By combined XPS and TOF-SIMS measurements, we can identify that oxide species in amorphous layer are mainly WO_3 and TeO with oxygen vacancies. By fitting the angle-dependent XPS spectra, obvious downward band bending can be observed after exposure to air. It confirms an electric field or polarization pointing to the bulk. We attribute such behavior to the pinned ionized donors from surface oxide species, which attract electrons from bulk and form the electric field. Surface band bending isn't found on freshly cleaved WTe_2 and fully oxidized surface. Our study here provides important insights about the surface polarization of WTe_2 and may also help to explain magnetotransport behavior after oxidation.

Methods

Sample preparation. WTe_2 crystal samples were purchased from PrMat (PrMat, China). The WTe_2 single crystal were stuck with a ceramic rod using Ag paste, and then loaded into ultra-high vacuum (UHV) chamber. The samples were cleaved *in-situ* in XPS chamber before ADXPS measurement. After the ADXPS measurement on fresh-cleaved WTe_2 , the samples were exposed to the air for different times (such as 1 min, 5 min, 2 h, 32 h here). After each exposure, the WTe_2 sample were immediately loaded into the XPS's UHV chamber and probed at the same location.

HRTEM characterization. The thickness of oxidation layer was characterized by using an *ex-situ* high resolution transmission electron microscopy (HRTEM) at room temperature on a Talos (FEI) setup with 200 keV voltage. Samples for the HRTEM characterizations were prepared by using focused ion beam (FIB) method after exposure to air for 32 hours. Pt protective layer was deposited to avoid physical damage during FIB process. The electron energy-loss spectroscopy (EELS) line profile and imaging were recorded across the oxide layer/ WTe_2 interface.

TOF-SIMS characterization. Time-of-Flight Secondary Ion Mass Spectrometry (TOF-SIMS) experiments were carried out with an IONTOF apparatus (TOF.SIMS 5-100), equipped with a Bi liquid metal ion source as the probe beam gun. Bi^+ ion beam with energy of 30 keV and current of 4.5 nA was used here. The depth profile was performed with 500 eV Cs^+ ion as sputtering source and a beam current of 5 nA.

ADXPS characterization. XPS measurements were carried out in an ultra-high vacuum (UHV, $\sim 5 \times 10^{-10}$ mbar) chamber, equipped with a hemispherical electron energy analyzer (PHI 5000, VersaProbe, ULVAC-PHI) and a monochromatic Al K_{α} X-ray source of 1486.7 eV. X-ray. Spot size of 100 μm diameter was adopted during high-resolution XPS spectra measurement. To probe the same position on the surface after each exposure, we used X-ray beam induced secondary electron imaging (SXI). With fixed hemispherical electron energy analyzer, the sample stage can be tilted to collect photoelectron from

different take-off-angles (TOA, θ , the elevation angle with respect to the sample surface), as shown in Fig. 1(b). The photoelectron escape depth λ equals to $\lambda_0 \sin \theta$, where λ_0 is the inelastic mean free path of photoelectrons. The binding energy (BE) of core-level peaks were calibrated with respect to the C-C 1s bond (BE = 284.8 eV). For freshly cleaved samples without C adsorption, the binding energy were calibrated with Au 4f_{7/2} emission line. The spectra are curve-fitted after subtracting a Shirley-type background.

An internal electrostatic potential, due to surface charge pinning or polarization, will induce band bending, which changes the measured value of core-level spectra under different TOAs. Based on the apparent binding energy and line shape in ADXPS measurements, surface band bending and internal potential gradient can be calculated.³³ The principle and calculation method have been specified previously.³³⁻³⁶ Briefly, a measured apparent core level spectrum is actually an integration of photoelectrons emitting from a depth of d_0 , and can be given by

$$I(E) = \int_0^{d_0} I_0(E, z) \exp(-z/\lambda) dz, \quad (1)$$

where z is the depth from the surface and $I_0(E, z)$ refers to the core level spectrum at each position. λ is the inelastic mean free path of photoelectrons at ϑ . When the internal electrostatic potential or surface band bending is not negligible, binding energy E is z -dependent and can be given as $E_0 - \phi(z)$. The $I_0(E - \phi(z), z)$ can be calculated by the pseudo-Voigt function as follows,³³

$$I_0(E - \phi(z), z) = I_{00} \left[\alpha \exp \left\{ -\ln 2 \frac{(E - \phi(z))^2}{(F/2)^2} \right\} + (1 - \alpha) \frac{1}{1 + \frac{(E - \phi(z))^2}{(F/2)^2}} \right] \quad (2)$$

where I_{00} , α , and F are the core level spectrum intensity, the ratio of Gaussian function, and the full width at half maximum (FWHM) of the core level spectrum, respectively. Due to the small depletion layer width, here we assume the electrostatic potential depends linearly on z . Quadratic approximation fitting results into large error. Then the binding energy can be given as $E_0 + Kz$, where E_0 is the binding energy at surface and K is the strength of the electrostatic potential.

Declarations

Acknowledgements

This work is supported by National Natural Science Foundation of China (Grants No. 11604366 and No. 11634007) and the National Natural Science Foundation of Jiangsu Province (Grants No. BK 20160397). F.-S. L. acknowledges support from the Youth Innovation Promotion Association of Chinese Academy of Sciences (2017370).

Author Contributions

F.L., and A.D. conceived and designed the experiments; A.C., H.L., R.H., Y. Z., Z. L., L. W., F. C., W. R., S. L., B. Y. performed sample preparation, XPS and HRTEM experiments; T. L. carried out FIB process for HRTEM experiment; R.H. performed TOF-SIMS experiment; F.L. wrote the paper. All the authors analyzed the data and edited the paper.

Additional Information

Competing Interests: The authors declare that they have no competing interests.

References

1. Ali, M.N., *et al.* Large, non-saturating magnetoresistance in WTe_2 . *Nature* **514**, 205-208 (2014).
2. Wang, Y., *et al.* Direct evidence for charge compensation-induced large magnetoresistance in thin WTe_2 . *Nano Lett.* **19**, 3969-3975 (2019).
3. Kang, K., Li, T., Sohn, E., Shan, J. & Mak, K.F. Nonlinear anomalous Hall effect in few-layer WTe_2 . *Nat. Mat.* **18**, 324-328 (2019).
4. Fatemi, V., *et al.* Electrically tunable low-density superconductivity in a monolayer topological insulator. *Science* **362**, 926 (2018).
5. Kang, D., *et al.* Superconductivity emerging from a suppressed large magnetoresistant state in tungsten ditelluride. *Nat. Commun.* **6**, 7804 (2015).
6. Pan, X.C., *et al.* Pressure-driven dome-shaped superconductivity and electronic structural evolution in tungsten ditelluride. *Nat. Commun.* **6**, 7805 (2015).
7. Sajadi, E., *et al.* Gate-induced superconductivity in a monolayer topological insulator. *Science* **362**, 922 (2018).
8. Tang, S.J., *et al.* Quantum spin Hall state in monolayer $1T'$ - WTe_2 . *Nat. Phys.* **13**, 683 (2017).
9. Wu, S., *et al.* Observation of the quantum spin Hall effect up to 100 kelvin in a monolayer crystal. *Science* **359**, 76-79 (2018).
10. Yan, B. & Felser, C. Topological materials: Weyl semimetals. *Annu. Rev. Condens. Matter Phys.* **8**, 337-354 (2017).
11. Soluyanov, A.A., *et al.* Type-II Weyl semimetals. *Nature* **527**, 495-498 (2015).
12. Chang, T.-R., *et al.* Prediction of an arc-tunable Weyl Fermion metallic state in $Mo_xW_{1-x}Te_2$. *Nat. Commun.* **7**, 10639 (2016).

13. Lv, Y.-Y., *et al.* Experimental observation of anisotropic Adler-Bell-Jackiw anomaly in Type-II weyl semimetal $\text{WTe}_{1.98}$ crystals at the quasiclassical regime. *Phys. Rev. Lett.* **118**, 096603 (2017).
14. Fei, Z., *et al.* Ferroelectric switching of a two-dimensional metal. *Nature* **560**, 336-339 (2018).
15. Xiao, J., *et al.* Berry curvature memory through electrically driven stacking transitions. *Nat. Phys.* (2020).
16. Sharma, P., *et al.* A room-temperature ferroelectric semimetal. *Sci. Adv.* **5**, 5080 (2019).
17. Chang, K., *et al.* Discovery of robust in-plane ferroelectricity in atomic-thick SnTe. *Science* **353**, 274-278 (2016).
18. Pletikoscic, I., Ali, M.N., Fedorov, A.V., Cava, R.J. & Valla, T. Electronic structure basis for the extraordinary magnetoresistance in WTe_2 . *Phys. Rev. Lett.* **113**, 216601 (2014).
19. Wu, Y., *et al.* Temperature-induced lifshitz transition in WTe_2 . *Phys. Rev. Lett.* **115**, 166602 (2015).
20. Di Sante, D., *et al.* Three-dimensional electronic structure of the type-II Weyl semimetal WTe_2 . *Phys. Rev. Lett.* **119**, 026403 (2017).
21. Wang, C.-L., *et al.* Evidence of electron-hole imbalance in WTe_2 from high-resolution angle-resolved photoemission spectroscopy. *Chin. Phys. Lett.* **34**, 097305 (2017).
22. Woods, J.M., *et al.* Suppression of magnetoresistance in thin WTe_2 flakes by surface oxidation. *ACS Appl. Mater. & Interf.* **9**, 23175-23180 (2017).
23. Li, J., Cheng, S., Liu, Z., Zhang, W. & Chang, H. Centimeter-scale, large-area, few-layer 1T'- WTe_2 films by chemical vapor deposition and its long-term stability in ambient condition. *J. Phys. Chem. C* **122**, 7005-7012 (2018).
24. Naylor, C.H., *et al.* Large-area synthesis of high-quality monolayer 1T'- WTe_2 flakes. *2D Mater.* **4**, 021008 (2017).
25. Liu, W.L., *et al.* Effect of aging-induced disorder on the quantum transport properties of few-layer WTe_2 . *2D Mater.* **4**, 011011 (2017).
26. Mleczko, M.J., *et al.* High current density and low thermal conductivity of atomically thin semimetallic WTe_2 . *ACS Nano* **10**, 7507-7514 (2016).
27. Ye, F., *et al.* Environmental instability and degradation of single- and few-Layer WTe_2 nanosheets in ambient conditions. *Small* **12**, 5802-5808 (2016).
28. Lee, C.H., *et al.* Tungsten ditelluride: a layered semimetal. *Sci. Rep.* **5**, 10013 (2015).
29. Yang, J., *et al.* Oxidation-induced topological phase transition in monolayer 1T'- WTe_2 . *J. Phys. Chem. Lett.* **9**, 4783-4788 (2018).
30. Alexander V. Naumkin, A.K.-V., Stephen W. Gaarenstroom, and Cedric J. Powell. NIST X-ray photoelectron spectroscopy database <http://srdata.nist.gov/xps/> **v4.1**(2012).
31. S. Tanuma, C.J.P.D.R.P. Calculations of electron inelastic mean free paths. V. Data for 14 organic-compounds over the 50–2000 eV range. *Surf. Interf. Anal.* **21**, 165–176 (1994).

32. C. J. Powell, A.J. NIST Electron Inelastic-Mean-Free-Path Database.
<https://www.nist.gov/system/files/documents/srd/SRD71UsersGuideV1-2.pdf> v1.2(2010).
33. Zhao, Y., *et al.* Precise determination of surface band bending in Ga-polar *n*-GaN films by angular dependent X-Ray photoemission spectroscopy. *Sci. Rep.* **9**, 16969 (2019).
34. Akazawa, M., *et al.* Measurement of valence-band offsets of InAlN/GaN heterostructures grown by metal-organic vapor phase epitaxy. *J. Appl. Phys.* **109**, 013703 (2011).
35. Akazawa, M. & Nakano, T. Valence band offset at Al₂O₃/In_{0.17}Al_{0.83}N interface formed by atomic layer deposition. *Appl. Phys. Lett.* **101**, 122110 (2012).
36. Ye, G., Wang, H. & Ji, R. Band alignment of HfO₂/AlN heterojunction investigated by X-ray photoelectron spectroscopy. *Appl. Phys. Lett.* **108**, 162103 (2016).

Figures

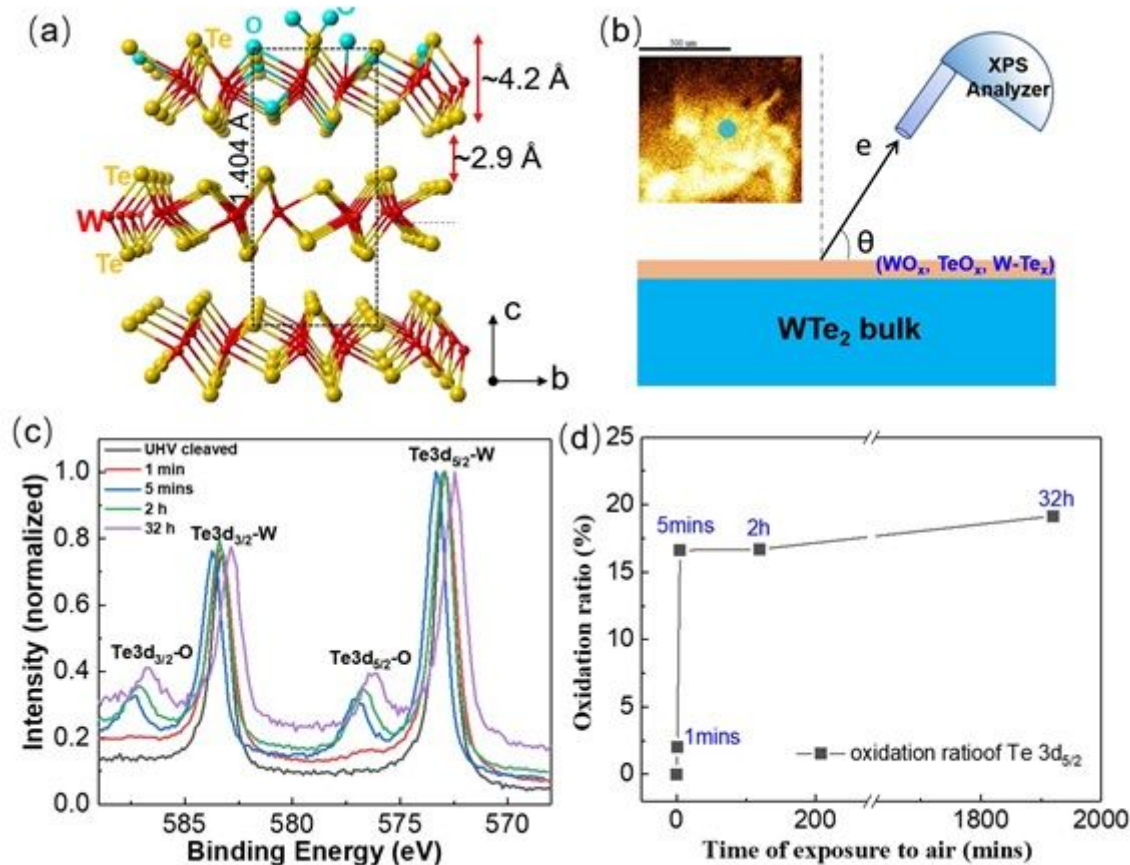


Figure 1

(a) Ball model of Td-WTe₂ with surface oxidation. (b) ADXPS measurement with TOA of θ on surface oxide layer containing WTe_x, WO_x, TeO_x. Circle in the inset marks the measured area in SXI image. (c) The normalized core level spectra of Te 3d after exposure to air for different times, collected at $\theta = 45^\circ$.

(d) The oxidation ratio as function of exposure time, calculated from the ratio of Te 3d5/2-O to Te 3d5/2-W.

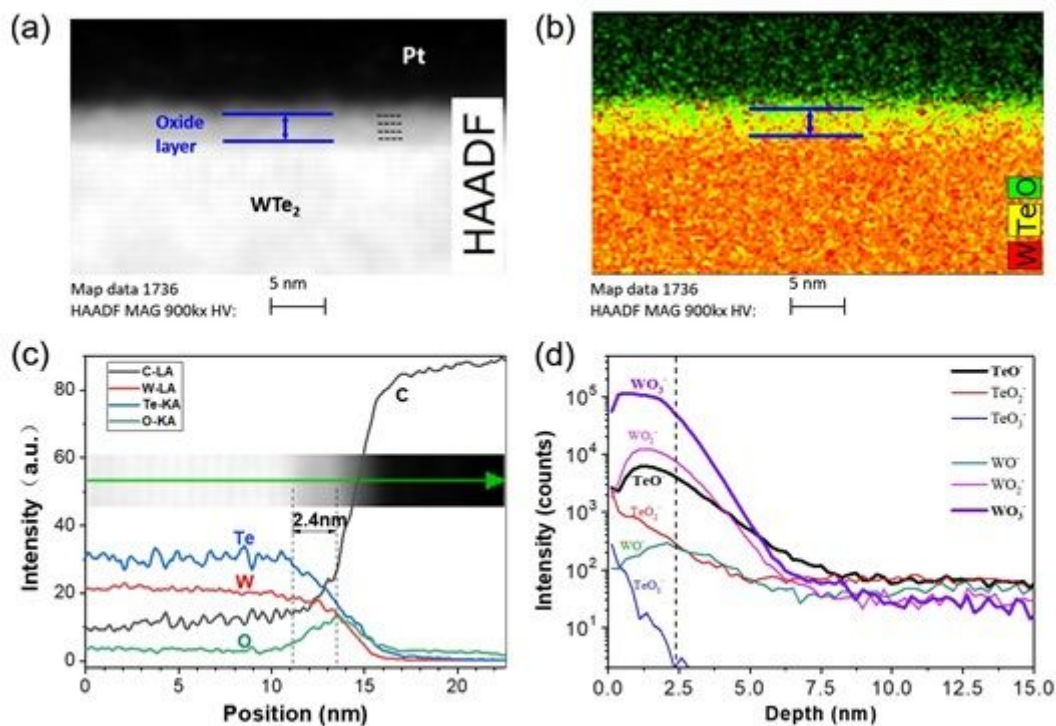


Figure 2

(a) The HAADF image of WTe₂ after exposure to air for 32 h during HRTEM measurement, showing amorphous oxidation layer on WTe₂ surface. (b) The corresponding EELS of W, Te and O mapping. (c) Line profile of EELS across surface oxide layer. The inset shows the measured location. (d) Depth profile measured by TOF-SIMS, showing spatial distribution of oxidation species.

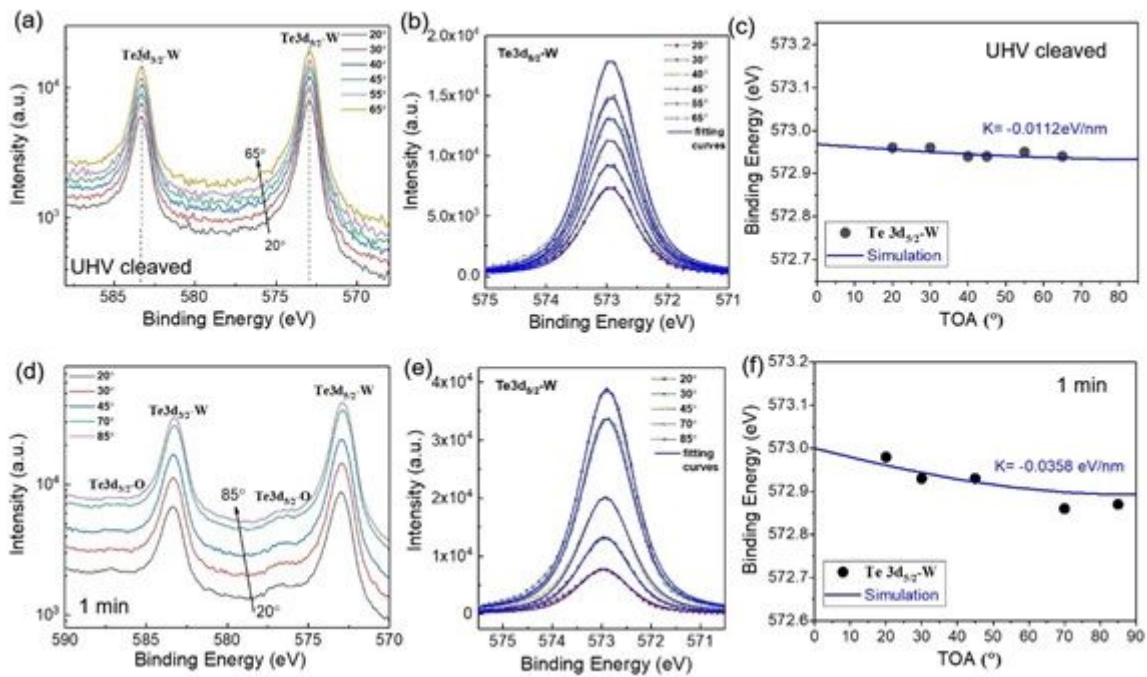


Figure 3

(a) XPS core level spectra of Te 3d on freshly cleaved sample, collected under various TOAs. (b) Measured (dashed lines) and fitted curves (solid lines) of Te 3d_{5/2}-W peaks after subtraction of Shirley background. (c) Measured (open circle) and simulated (red solid line) binding energy of Te 3d_{5/2}-W at different TOAs on freshly cleaved sample. (d) XPS core level spectra of Te 3d on WTe₂ after exposure to air for 1 minute, Te-O bond can be clearly observed. (e) Measured (dashed lines) and fitted curves (solid lines) of Te 3d_{5/2}-W peaks after subtraction of Shirley background. (f) Measured (open circle) and simulated (red solid line) binding energy of Te 3d_{5/2}-W on one-minute sample.

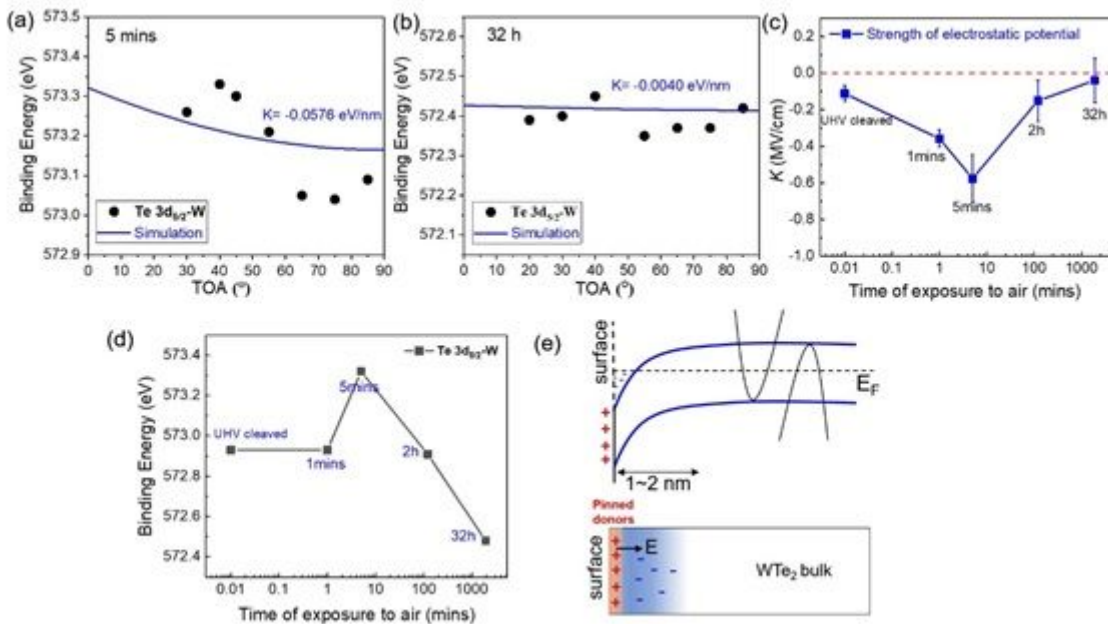


Figure 4

Measured (open circle) and simulated (red solid line) binding energy of Te 3d_{5/2}-W after exposure to air for 5 mins (a) and 32 h (b), respectively. (c) The obtained strength of electrostatic potential K after fitting. (d) The binding energy of Te 3d_{5/2}-W obtained at $\theta = 45^\circ$. (e) Schematic diagram of surface downward band bending, showing pinned ionized donor and built-in electric field.